

Review

Magnetic Shape Memory Microactuators

Manfred Kohl *, Marcel Gueltig †, Viktor Pinneker †, Ruizhi Yin †, Frank Wendler † and Berthold Krevet †

Institute of Microstructure Technology, Karlsruhe Institute of Technology (KIT), Postfach 3640, 76021 Karlsruhe, Germany; E-Mails: marcel.gueltig@kit.edu (M.G.); viktor.pinneker@kit.edu (V.P.); ruizhi.yin@kit.edu (R.Y.); frank.wendler@kit.edu (F.W.); berthold.krevet@kabelbw.de (B.K.)

† These authors contributed equally to this work.

* Author to whom correspondence should be addressed; E-Mail: manfred.kohl@kit.edu; Tel.: +49-721-6082-2798; Fax: +49-721-6082-4331.

External Editor: Ulrike Wallrabe

Received: 29 September 2014; in revised form: 1 November 2014 / Accepted: 1 November 2014 / Published: 18 November 2014

Abstract: By introducing smart materials in micro systems technologies, novel smart microactuators and sensors are currently being developed, e.g., for mobile, wearable, and implantable MEMS (Micro-electro-mechanical-system) devices. Magnetic shape memory alloys (MSMAs) are a promising material system as they show multiple coupling effects as well as large, abrupt changes in their physical properties, e.g., of strain and magnetization, due to a first order phase transformation. For the development of MSMA microactuators, considerable efforts are undertaken to fabricate MSMA foils and films showing similar and just as strong effects compared to their bulk counterparts. Novel MEMS-compatible technologies are being developed to enable their micromachining and integration. This review gives an overview of material properties, engineering issues and fabrication technologies. Selected demonstrators are presented illustrating the wide application potential.

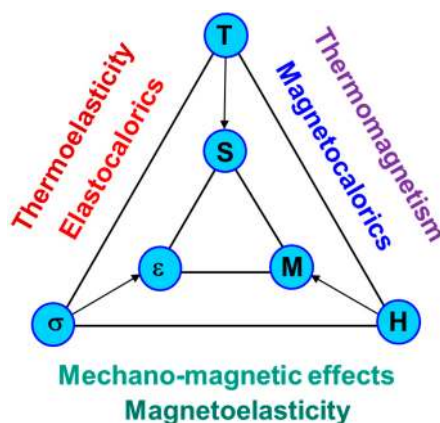
Keywords: microsystems technology; microactuation; smart materials; ferromagnetism; shape memory alloys; thin films

1. Introduction

Magnetic shape memory alloys (MSMAs) belong to the class of Heusler materials, which are ordered intermetallics with the generic formula X_2YZ with X and Y being 3D elements and Z a group IIIA–VA element [1]. The three elements occupy the crystallographically non-equivalent positions of an L_{21} structure. An important example is Ni_2MnGa , which shows magnetism mainly due to the Mn atoms. MSMAs exhibit pronounced magnetic ordering and large magnetocrystalline anisotropy resulting in energetically preferred orientation of magnetic moments. In addition, MSMAs undergo a first-order martensitic phase transformation, which involves a large, abrupt change in both structural and magnetic properties. The phase transformation proceeds in a reversible manner, enabling the thermal shape memory effect as well as superelasticity.

The presence of coupled ferromagnetic and metastable ferroelastic (martensitic) domains in MSMA materials gives rise to multiferroic properties. As illustrated in Figure 1, generally any change of one of the physical properties induced by an external stimulus causes characteristic changes of the other physical properties. Owing to their multiferroic coupling properties, FSMAs (Ferromagnetic shape memory alloys) exhibit various modes of combined sensing and actuation capabilities [2]. As a consequence, MSMA actuators may only consist of a single piece of material, but still may perform several functions. Therefore, the underlying philosophy of actuation by smart materials may be summarized by saying that “the material is the machine!” [3]. MSMA materials offer different options to induce a change in the mechanical properties that could be used for actuation. One example is the effect of magnetic field-induced reorientation (MIR) of martensite, which is the underlying coupling mechanism of the magnetic shape memory (MSM) effect that was discovered in 1996 [4]. Also, the inverse mechano-magnetic effect of strain-induced change of magnetization has been reported allowing for intrinsic strain sensing [5]. Besides magneto-mechanical coupling, MSMAs also exhibit large mechano-caloric [6], magneto-caloric [7], and magneto-resistance effects [8].

Figure 1. Scheme of the coupling between thermal, mechanical, and magnetic properties in multiferroic materials. Legend: T, temperature; S, entropy; σ , stress; ϵ , strain; H, magnetic field; M, magnetization.



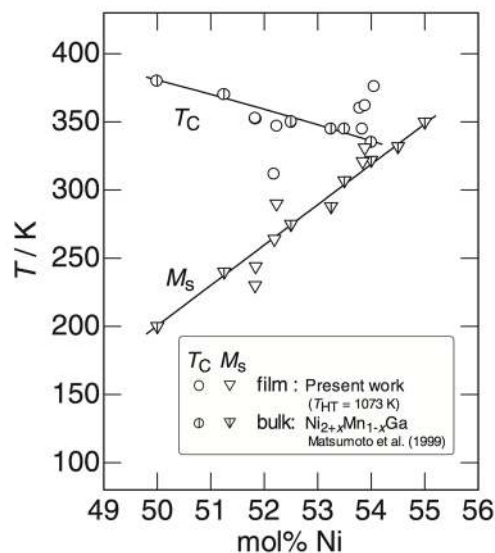
Using the multifunctional properties of MSMAs is particularly interesting for applications in small dimensions. Recent efforts in miniaturization of MSM actuators follow a top-down approach by thinning bulk single crystals to foil specimens [2,9,10]. An alternative is MSMA films that are

fabricated in a bottom-up manner by film deposition [11–14]. From a technological point-of-view, this approach is the most suitable for the development of integrated MEMS devices. The technology issues of combining MSMA materials and MEMS will be discussed in Section 2. In Section 3, we present recent developments of MSMA actuators based on film and foil specimens. This review focuses mainly on the non-stoichiometric Heusler alloy Ni–Mn–Ga. However, many of the presented concepts could be easily adapted to other MSMA materials.

2. Combining MSMA Materials and MEMS Technologies

MSMA materials that are suitable for applications should undergo the martensitic phase transformation above ambient temperature. Phase transformation temperatures and martensitic phases observed in non-stoichiometric $\text{Ni}_{2-x}\text{Mn}_x\text{Ga}_y$ single crystals are strongly dependent on the chemical composition. As shown in Figure 2, the martensitic phase transformation temperature M_s strongly increases for increasing Ni-content, while the Curie temperature T_C shows a slight decrease. This behavior is in line with the Hume–Rothery rule that relates the increase of phase transformation temperature to an increase of the valence electron concentration [15]. At the intersection of T_C and M_s , the crystal structure of the martensite changes from modulated to non-modulated phase. The nearly tetragonal 10M and orthorhombic 14M modulated martensite phases are stable for chemical compositions having low valence electron concentration ea below 7.7 [16]. For high valence electron concentration $ea > 7.7$, the tetragonal non-modulated (NM) phase is observed. In order to enable the MSM effect, the critical stress to induce reorientation of martensite should be below 2 MPa [17]. In Ni–Mn–Ga, only the modulated martensite phases show such low twinning stress. Therefore, starting materials for the development of MSMA microactuators, using the MSM effect, are single crystalline Ni–Mn–Ga foils and epitaxial Ni–Mn–Ga films with modulated martensite phase at room temperature. For thermal and magnetostatic actuation, also polycrystalline Ni–Mn–Ga foils and films with modulated or non-modulated martensite phase are suitable.

Figure 2. Start temperature of martensitic transformation M_s and Curie temperature T_C as a function of Ni content for Ni–Mn–Ga bulk and thin film materials. Reprinted with permission from [18], copyright 2000 IOS Press.



2.1. MSMA Foils

Single crystalline MSMA foils are prepared by cutting thin plates from a bulk single crystal, e.g., by wire sawing. Subsequent thinning to the desired thickness is performed by a series of mechanical and chemo-mechanical polishing steps [9] or grinding and electrochemical polishing [10]. Minimum foil thicknesses have been prepared down to about 50 μm . Technological challenges are related to the minimization of surface defects created during foil fabrication. The material properties that are obtained fulfill the requirements for MIR with high magneto-strain and thus open up the opportunity to develop miniature MSM actuators. However, this approach is hardly suitable for large scale production as it is quite labor-intensive and involves a large material consumption.

2.2. MSMA Films

Sputtering is the most favorable deposition method to obtain thick films on a large scale as required for MEMS technology [2,14]. The resulting film structure depends on various parameters including substrate, deposition temperature, sputtering power, and annealing conditions. Consequently, as-prepared films can exhibit polycrystalline structure [18–24] or an epitaxial relation to the substrate [11–14,25–28].

A process has been developed for fabrication of freestanding polycrystalline Ni–Mn–Ga films showing 10 M martensite at room temperature [18,21]. Film deposition has been performed on polyvinylalcohol (PVA) substrates that can be dissolved after sputtering. The sputtering power is varied between 50 and 200 W, the Argon gas flow is maintained at $230 \text{ mm}^3 \cdot \text{s}^{-1}$, and the substrate temperature is kept at 50 °C. Under these conditions, as-deposited films are amorphous and require a heat treatment to adjust the crystal structure and phase transformation properties. The effect of heat treatment on the performance of polycrystalline Ni–Mn–Ga films is described in [18].

As epitaxial films are the counterpart to bulk single crystals, they are most interesting for the realization of MSM actuation on a small scale. Details on the preparation of epitaxial Ni–Mn–Ga films by magnetron sputtering can be found in [14]. A MnO substrate with [100] orientation is used with an intermediate Cr-layer in order to minimize the lattice mismatch. After deposition, the Cr layer can be chemically removed to obtain freestanding epitaxial films. These films show a high pseudo-plastic strain of more than 12% [29]. However, despite many efforts, MSMA films that have been produced by magnetron sputtering up to now exhibit too large twinning stresses inhibiting the MSM effect. Major challenges are related to the control of phase formation and microstructure during film deposition [14]. Different thermo-magneto-mechanical training methods have been investigated to improve the microstructure of as-deposited films [14] and thinned foils [9] in order to reduce the twinning stress and improve TB (Twin boundary) mobility. Instead of using the MSM effect for actuation, a number of alternative actuation concepts have been investigated as will be discussed in Section 3.

2.3. Integrated MSMA Film and Foil Microstructures

One of the main advantages of MEMS technology is parallel processing and structuring of many microparts on the wafer scale. However, parallel fabrication of (M)SMA materials in batches is hampered by material and process incompatibilities. For example, the thermo-mechanical treatment required to adjust microstructure and phase transformation properties encounters incompatibilities with

most other materials used in microsystems. In addition, chemical micromachining requires strong etchants in a highly selective process. Therefore, initial attempts to fabricate and integrate (M)SMA materials in MEMS were based on pick-and-place procedures and assembly of individual components. In the meantime, these technology barriers have been overcome by the development of wafer-level bonding and release technologies for (M)SMA films that allow for parallel processing of critical steps on different substrates [30,31].

A typical process based on optical lithography and wet-chemical etching is summarized in Table 1 following previous work on batch fabrication of SMA materials. In the first step, the freestanding MSMA film/foil is bonded on a substrate prior to micromachining. This can be performed by a sacrificial bonding layer [30,32]. To obtain freely movable structures for actuation, the bonding layer should be chemically dissolvable. Subsequent steps include the fabrication of a hard mask, lithography, and etching of the MSMA film/foil. Thus, by combining film/foil integration, micromachining and sacrificial layer technology, fully integrated MSMA microactuators can be fabricated in a MEMS compatible manner at low cost. Figure 3 shows, for instance, an array of batch-fabricated SMA film microstructures on a silicon wafer.

Table 1. MEMS-compatible process flow for fabrication of (magnetic) shape memory alloys ((M)SMA) microactuators.

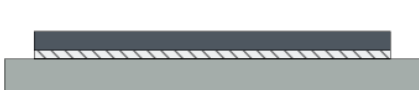

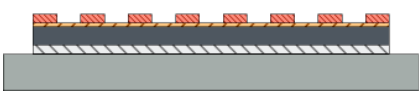
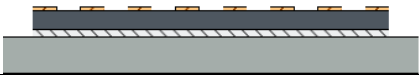
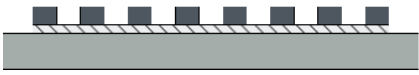
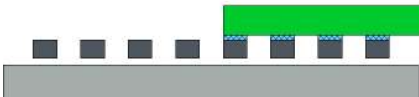
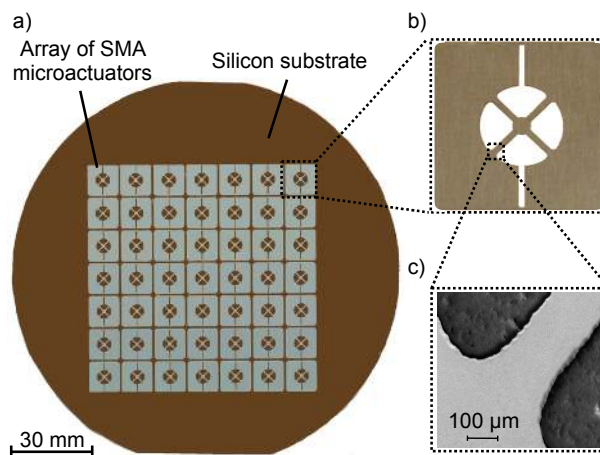
 <p>MSMA Sacrificial layer Substrate</p>	<p>The freestanding MSMA film/foil is bonded onto a silicon substrate (bonding layer). Alternatively, the MSMA film is deposited by magnetron sputtering on a buffer layer.</p>
 <p>Gold</p>	<p>A gold layer is sputtered onto the MSMA layer for use as a hard mask.</p>
 <p>Photoresist</p>	<p>Optical lithography: A positive resist is spin coated onto the Au layer, exposed by UV light, and developed.</p>
	<p>The Au hard mask is patterned by wet chemical etching via the resist mask.</p>
	<p>The MSMA layer is micromachined by wet-chemical etching (e.g., hydrofluoric acid, nitric acid, and deionized water [33]). The hard mask is removed afterwards.</p>
 <p>Carrier substrate Bonding layer</p>	<p>Free-standing MSMA microactuators are released from the substrate by selective removal of the sacrificial layer. The microactuators may be selectively transferred to another substrate by bonding and release technology [30,31].</p>

Figure 3. (a) Array of SMA film microstructures on a silicon substrate covered by a sacrificial layer; (b) Magnified photograph of a single SMA microactuator; (c) Scanning electron microscope (SEM) picture of a single SMA beam. Reprinted with permission from [33], copyright 2014 IOP Science.



3. Actuation Principles and Demonstrators

Table 2 summarizes different actuation mechanisms and the underlying coupling effects. In the following, these actuation mechanisms will be described in more detail, and recent efforts in development of first demonstrators will be presented.

Table 2. Mechanisms for magnetic shape memory actuation and underlying coupling effects.

Coupling effect	Actuation mechanism	Reference
Magnetic field-induced reorientation (MIR) of martensite	Magnetic shape memory (MSM) actuation	[4]
Temperature gradient-induced martensitic transformation	Single phase boundary actuation	[34]
Thermally induced ferromagnetic transition and martensitic transformation	Bidirectional magnetostatic and thermoelastic actuation	[35]
Thermally induced metamagnetic transition	Thermomagnetic actuation	[36]
Magnetic stray-field-induced microstructure	Magnetic stray-field induced actuation	[37]

3.1. Magnetic Shape Memory Actuation

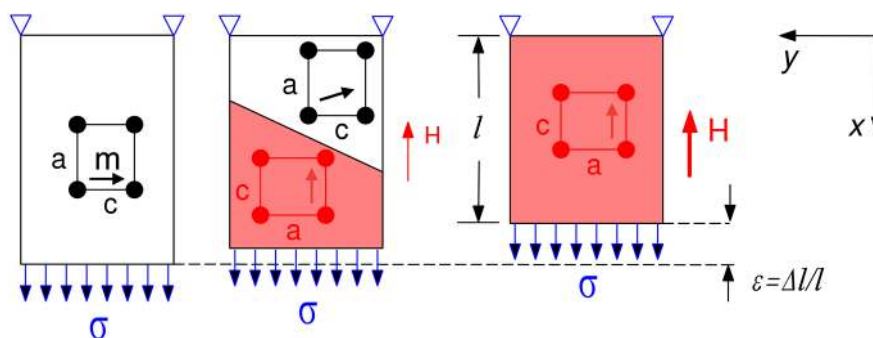
3.1.1. Operation Principle

In martensitic state, the crystallographic variants form a metastable system of structural domains that are separated by twin boundaries. In addition, magnetic domains of spontaneously aligned magnetic moments are present, and are oriented along the crystallographic easy direction due to magnetic anisotropy. The structural domains are strongly coupled to the magnetic domains. Under these conditions, the magnetic moments can align with respect to the magnetic field direction by reorientation of martensite variants once the magnetic field exceeds a critical value as sketched in Figure 4. Thereby, martensite variants with favorable orientation of magnetic easy axis grow with

respect to an external magnetic field, while unfavorably oriented variants shrink in size. The corresponding maximum reorientation strain is given by the difference of the involved lattice constants. This effect of magnetic field-induced reorientation (MIR) occurs by twin boundary motion, the critical field strength for MIR being determined by the mobility of twin boundaries.

In the Ni–Mn–Ga material system, modulated nearly tetragonal 10M, orthorhombic 14M and non-modulated (NM) tetragonal single crystal structures show maximum reorientation strains of 6.2%, 10.7% and 21%, respectively [38]. In particular, for the 10M modulated structure, twin boundary mobility can be exceptionally high at room temperature allowing for MIR at low critical magnetic field of $25 \text{ kA}\cdot\text{m}^{-1}$ corresponding to a twinning stress of only 0.1 MPa [39]. Compared to the thermal shape memory effect, MIR occurs at much faster time scales below 1 ms [40–42]. Therefore, the MSM effect has a large potential for high-stroke dynamic actuation. Among the investigated alloys, near stoichiometric Ni–Mn–Ga-based alloys exhibit exceptional actuation performance including reversible magneto-strains up to 12% when exposed to a moderate magnetic field [43]. However, the driving force of MIR is limited by the magnetic anisotropy energy K . If the stress becomes too large, exceeding the so-called blocking stress, magnetic moments can overcome K and align along the field direction simply by rotation due to the competing Zeeman effect. In Ni–Mn–Ga, for instance, the maximum stress that can be generated by the magnetic field is restricted to a few MPa [44].

Figure 4. Schematic operation principle of the MSM effect for a 10M Ni–Mn–Ga film/foil actuator. Applying a tensile stress generates an initial single crystalline state with the long a -axis being aligned along the tensile (x -)direction. For increasing magnetic field along the x -direction, variants with short c -axis along this direction nucleate and grow in size until a fully reoriented single crystalline state is formed. The resulting length change $\Delta l/l$ corresponds to the difference of lattice constants $(c-a)/c$. m , magnetic moment; H , magnetic field; σ , tensile stress. Reprinted with permission from [45], copyright 2011 IOP Science.



3.1.2. Simulation of MSM Actuation

Different simulation models have been developed to predict the strain and force output of MSM actuators as a function of external magnetic field [46–51]. Here, we present a brief sketch of a thermodynamic model that considers three possible variants of a Ni–Mn–Ga single crystal with tetragonal 10M martensite structure [52,53]. The model has been implemented into a FEM (Finite element method) code to predict the MIR effect in linear actuators based on MSMA foils that are subjected to different loading conditions and mechanical constraints [53–57]. The finite element software includes an integral magnetic solver and applies classical beam theory for solid mechanics.

By taking into account the energy terms of mechanical, magnetic anisotropy, Zeeman, and magnetostatic energy, the combined effects of stress, temperature, and magnetic fields on the fractions of martensite variants and austenite can be described. The mechanical energy contribution is formulated connecting two energy minima corresponding to the two possible variant orientations under consideration. The magnetic anisotropy contribution reads:

$$\Psi_{\text{anis}}(\mathbf{M}) = K \sin^2(\alpha_c - \alpha) \quad (1)$$

where K denotes the anisotropy constant and α_c denotes the angle of magnetic moment with respect to the initial variant ($\alpha_c = 0$ for M_1 , and $\alpha_c = \pi/2$ for M_2 or M_3). The Zeeman energy describes the energy of the magnetization M in an external field:

$$\Psi_{\text{Zeeman}}(\mathbf{M}, \mathbf{B}) = -MB \cos(\alpha_B - \alpha) \quad (2)$$

with α and α_B being the angles of magnetization and external magnetic field with respect to the easy axis in initial state. The magnetostatic energy is given by:

$$\Psi_{\text{demag}}(\mathbf{M}) = -\frac{1}{V} \int \frac{1}{2} \mu_0 \mathbf{M} \mathbf{H}_{\text{demag}} dV = \frac{1}{2} \mu_0 \mathbf{M} \cdot \mathbf{N} \mathbf{M} \quad (3)$$

where the integral extends over the total active material volume. The demagnetization field $H_{\text{demag}} = -\mathbf{N} \cdot \mathbf{M}$ is calculated by applying the demagnetization tensor N , assuming a homogeneous magnetization. The minima of the total Gibbs free energy determine the equilibrium conditions. The direction of applied magnetic and stress field defines the position of the minima and hence determines which of the three possible martensite variants contribute to the reorientation. Variant reorientation is described as a thermally activated process in the energy landscape depending on strain and orientation of magnetic moment. A typical energy landscape is depicted in Figure 5 showing two minima that can be tuned by applying an external magnetic field.

3.1.3. MSM Linear Actuators

Novel MSM linear actuators have been developed using the MIR effect in single crystalline 10M Ni–Mn–Ga foils [45,54]. Typical foil thicknesses have been in the range of 100–200 μm . In this case, uniaxial tensile loading is used to adjust the initial state as compression loading would cause buckling perpendicular to the foil plane. In contrast to compression loading, however, two coexisting martensite variants with c -axes perpendicular to the tensile direction can be formed, which may reduce the maximum achievable shape change of 6% [45]. Based on theoretical considerations, the critical magnetic field for MIR is expected to decrease for decreasing foil thickness [10]. However, in real foil specimens, the critical magnetic field and maximum magnetostrain are affected by material inhomogeneity and surface defects depending on the technology of foil fabrication as well as by the constraints of fixation and tensile loading [34,45]. The influence of defects on the mobility of twin boundaries can be reduced by training of the MSMA material. Different methods of thermo-magneto-mechanical training have been developed and their effect on magneto-strain and stress-strain characteristics have been investigated [9,34].

In order to generate reversible actuation cycles, a reset mechanism has to be implemented. In general, resetting could be achieved by applying a second magnetic field in perpendicular direction with respect to the initial field for MIR or by applying a mechanical biasing load as illustrated in

Figure 4. In a practical device, mechanical biasing can be easily implemented by a suitable tensile spring. Figure 6 shows a schematic of this type of MSM linear actuator. The main actuator components are a MSMA stripe, a non-magnetic reset spring, an interconnection between these components and a supporting frame. First, the MSMA stripe and tensile spring are preloaded by shifting one end of the supporting frame as illustrated in Figure 6b. As indicated in the inset, the MSMA stripe should be in a single variant state with the long a -axis being aligned along the tensile loading direction. When the external magnetic field B is applied in tensile direction, the c axis aligns along B through variant reorientation causing the stripe specimen to contract. After switching the magnetic field off, the initial state is restored by the spring.

Figure 5. Gibbs free energy depending on strain and the angle α of magnetic moment with respect to the initial orientation of easy axis. (a) A tensile stress of 1.5 MPa is applied, while the magnetic field is zero; (b) A magnetic field of 0.2 T is applied, while the external stress is zero. Depending on the applied magnetic field and stress, the global energy minimum switches orientation of magnetic moment by $\pi/2$ and strain by $\Delta\varepsilon = 0.06$ corresponding to variant reorientation. Reprinted with permission from [45], copyright 2011 IOP Science.

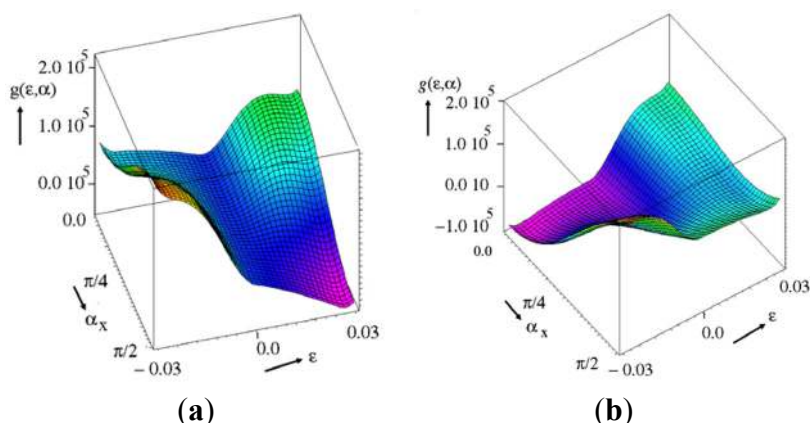
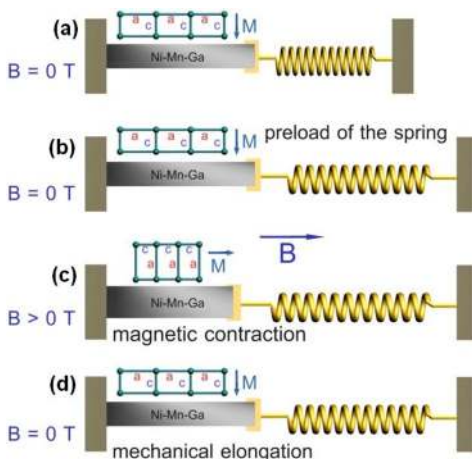
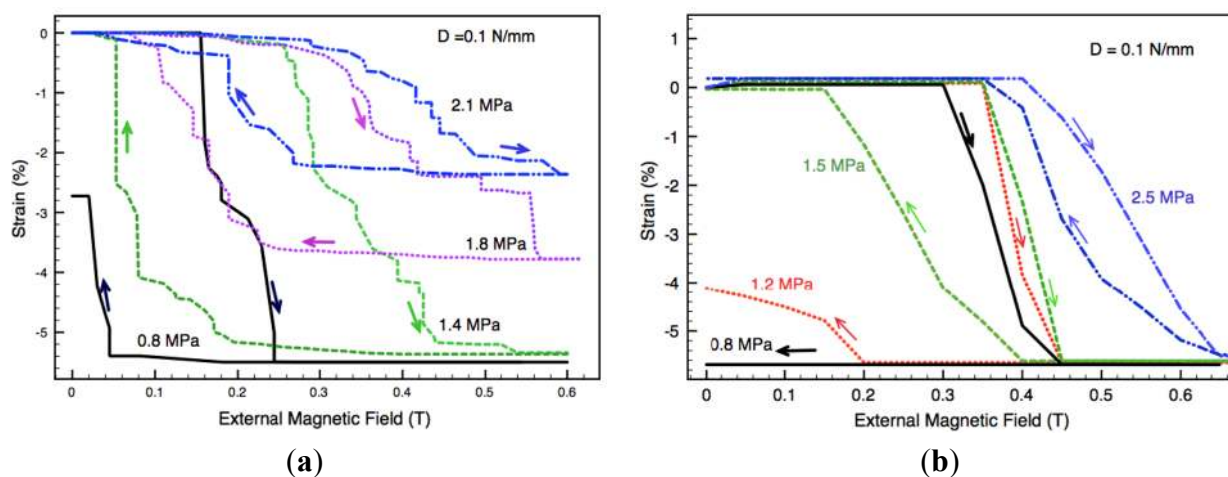


Figure 6. Schematic actuation cycle of the MSM linear actuator. (a) Load-free condition; (b) initial single variant state after mechanical preloading; (c) MSM actuation by an external magnetic field; (d) reset motion. Typical dimensions of MSMA foils are 6–15 mm in length and 2–3 mm in width. Reprinted with permission from [58], copyright 2012 WFB Wirtschaftsförderung Bremen GmbH.



Experimental and simulated magnetostrain characteristics of the MSM linear actuator are shown in Figure 7 for different levels of prestress. At zero load only a small critical magnetic field of 0.16 T is needed for reorientation. However, by foil contraction, the stress of the spring does not increase enough during MSM actuation to enable complete resetting. This demonstrates that sufficient preloading is mandatory to achieve complete actuation cycles. For a prestress of 1.4–1.6 MPa, a maximum reversible magnetostrain of 5.3% is found. In this case, magnetic field and biasing force allow for complete variant reorientation and resetting, respectively. The achieved magnetostrain is lower than the maximum possible value of 6% due to the constraints imposed by fixation and loading causing inactive parts that do not contribute to the MSM effect. At higher levels of prestress approaching the blocking stress of the material, the output stroke is reduced significantly. This effect is also reproduced by the simulation model, but it occurs very abruptly above 1.5 MPa as long as homogeneous material behavior is assumed. The tensile spring generates an additional stress increase during contraction of the actuator, which must not exceed the blocking stress. FEM simulations for the optimum prestress of 1.5 MPa indicate that this condition is fulfilled as long as the spring constant is below $0.5 \text{ N}\cdot\text{mm}^{-1}$ [54].

Figure 7. Experimental (a) and simulated (b) magneto-strain characteristics of a MSM linear actuator for different values of pre-stress as indicated. The twinning stress for the simulated homogenous material is 2 MPa. The linear actuator consists of a Ni–Mn–Ga stripe of $14 \times 3 \times 0.1 \text{ mm}^3$ and a tensile spring of Cu–Sn having a spring constant of $0.1 \text{ N}\cdot\text{mm}^{-1}$. The magnetic field is not corrected for demagnetization. Reprinted with permission from [54], copyright 2012 IOP Science.



As the jump-like nature of twin boundary motion gives rise to highly nonlinear and hysteretic magnetostrain characteristics, MSM linear actuators appear to be less suitable for positioning applications. However, the actuator geometry and intrinsic material properties such as the magnetization and electrical resistance are correlated with the specific set of variant volume fractions. Therefore, measurement of intrinsic material properties during actuation can be used for position sensing and control. It has been demonstrated, for instance, that the change of electrical resistance of a bulk single crystalline Ni–Mn–Ga actuator directly correlates with the change of geometric dimensions and, thus, with the magnetostrain [59]. As a consequence, hysteresis-free resistance-magnetostrain relations are

obtained. This indicates that the anisotropy of the electrical resistivity along the different crystallographic directions can be neglected [60,61]. Another experiment demonstrated that the inductance of a pick-up coil at the MSMA actuator may also be used for position sensing with good accuracy [62].

3.2. Single Phase Boundary Actuation

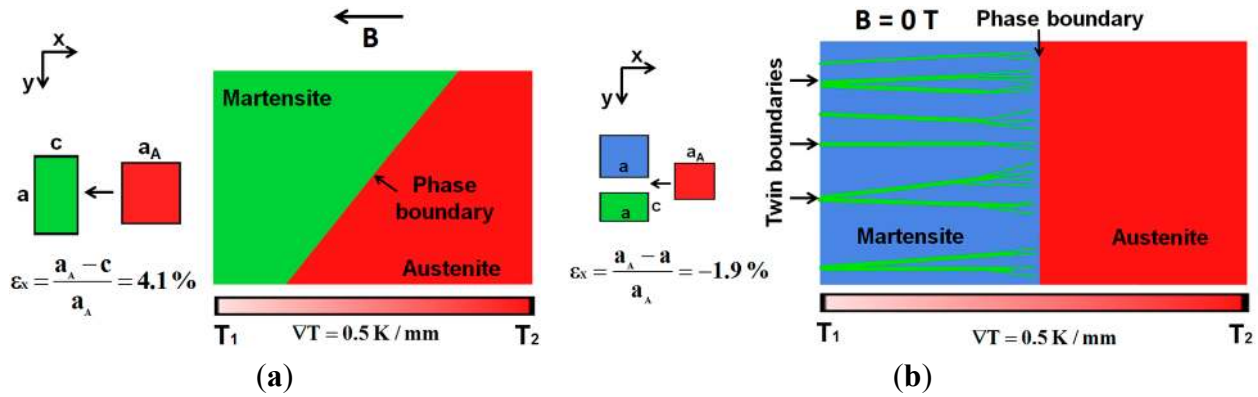
For decreasing size, tailoring the formation of modulated martensite phase and limiting the influence of defects becomes increasingly difficult due to technological constraints in fabrication of MSMA foils and films. Consequently, twinning stress and corresponding critical magnetic field become too high, preventing MSM actuation. Different schemes of stress assistance or increasing the operation temperature have been proposed to enable or improve MSM actuation by reducing the energy barrier for MIR. As a drawback, the overall complexity of the actuator device increases and miniaturization remains limited. Recently, it has been shown that thermal actuation by applying a temperature gradient could be an interesting alternative approach as it allows controlling the location of phase nucleation and the propagation of phase front [34].

3.2.1. Operation Principle

Starting materials in the following investigation are single crystalline MSMA foils. In general, the actuation mechanism also works for polycrystalline MSMA foils and films even though the effect size might be reduced. Figure 8 shows a schematic of a Ni–Mn–Ga foil that is subjected to a thermal field gradient along the x -direction. An additional magnetic field may be applied in the same (x -) or perpendicular (y -)direction. When increasing the temperature T_2 at the hot side above the martensite-austenite transformation temperature, austenite formation first starts at the energetically preferred hot side and then, upon further heating, continues along x -direction from the hot to the cold side by propagation of a single phase boundary. Propagation of the phase boundary occurs in a reversible manner, *i.e.*, back propagation of the phase boundary from cold to hot side occurs, when the temperature at the hot side T_2 is decreased again. Thus, the actuation strain resulting from the difference of lattice constants upon phase transformation can be controlled reversibly as well. At the phase front, tetragonal martensite may form with different orientations as illustrated in Figure 8b. However, only those variants or combinations of variants are formed that allow keeping the lattice strain at the phase boundary at a minimum. By applying an additional biasing magnetic field along x -direction B_x , only one martensite variant is energetically favored with the magnetic easy axis (c -axis) being oriented along B_x . In this case, single phase boundary actuation results in the formation of a single variant martensite state similar to the case of MSM actuation. As illustrated in the inset of Figure 8a, the maximum strain response is given by the difference of the short c -axis of tetragonal martensite and the axis of cubic austenite to be 4.1% [34]. Similarly, the magnetic field may be applied in a perpendicular direction to the thermal field gradient resulting in a smaller strain change of -1.9% that is given by the difference of the long a -axis of tetragonal martensite and the axis of cubic austenite [34].

In the case of incomplete reverse transformation to austenite, the remaining oriented martensite gives rise to an interesting historical effect. In this case, the biasing magnetic field is only required in the first actuation cycle. Subsequent actuation cycles do not need any biasing magnetic field to achieve reversible actuation with the same magnetostrain.

Figure 8. Schematic of single phase boundary actuation. A temperature gradient is generated along the x -direction, e.g., by local heating of the substrate. (a) In addition, a magnetic field is applied along the x -direction. (b) Reversible single phase boundary actuation for zero magnetic field. Reprinted with permission from [34], copyright 2014 Elsevier.



3.2.2. Mechanical Performance

In situ digital image correlation (DIC) measurements have been performed in order to investigate the effect of a temperature gradient during phase transformation on the evolution of strain. DIC reveals the local strain on the mesoscopic (μm) scale. Figure 9a shows a local strain-temperature characteristic that has been determined for a test area of a Ni–Mn–Ga specimen of $100\ \mu\text{m}$ thickness, as indicated in the inset. A small biasing magnetic field of $0.12\ \text{T}$ is applied along the length (x -)direction of the specimen. In addition, two series of strain maps are shown that have been recorded in the test area upon heating and cooling. The average local strain values are determined by taking the average value of each strain map. Upon heating, a single martensite–austenite phase front is observed that propagates from right to left through the test area, starting at a temperature of $58\ ^\circ\text{C}$. The phase front is oriented by a certain angle that is determined by the difference of lattice constants and strain minimization at the phase boundary [34]. The phase front divides the specimen into two regions, showing either zero or maximum change of strain in the order of 3.8% , indicating almost complete phase transformation from single variant martensite to austenite. The fluctuations within the two regions are due to pixel errors resulting from local changes of surface reflection that affect a deviation from the expected maximum possible strain change of 4.1% . This result is achieved for a rather small temperature gradient of only $5\ \text{K}\cdot\text{mm}^{-1}$. As illustrated in the inset, this temperature gradient has been realized by keeping a small distance between samples and heating substrate. The phase front moves through the entire specimen, starting at the fixed end with higher temperature T_2 to the freestanding end with temperature T_1 . Upon cooling, a single phase front occurs that propagates in the opposite direction. Similar observations are made by applying a magnetic field in a perpendicular (y -)direction [34].

If the biasing magnetic field is switched off, single phase boundary actuation is also observed, even though single variant martensite is no longer formed. As can be observed in the measurement shown in Figure 9b, reversible actuation cycles are present. In this case, heating induces a contraction of the specimen in the longitudinal (x -)direction by about -1.8% similar to the case of a biasing magnetic field in y -direction. However, a different orientation of phase boundary occurs indicating that different martensite variants are formed during phase transformation.

As single phase boundary actuation is based on a thermal actuation principle, it is not limited by the level of twinning stress and a low blocking stress. Thus, it opens up a route to realize MSMA actuation with large work output at low or even without magnetic field.

3.2.3. Thermal Linear Actuators

The similarities between single phase boundary and MSM actuation and the option for reversible control of phase boundary location suggest its use for linear positioning applications. The actuator setup and a photo of a first demonstrator are depicted in Figure 10. The Ni–Mn–Ga specimen is placed in the gap of a magnetic circuit that is excited by miniature permanent magnets. A small electrical heating element is bonded to the fixed end of the specimen, which thus determines the hot side with temperature T_2 . Heat conduction and convection give rise to a temperature gradient along the specimen, which is monitored at the specimen surface by an infrared camera. In the present case, the temperature gradient is about $3.3 \text{ K}\cdot\text{mm}^{-1}$ at a temperature T_2 of $100 \text{ }^\circ\text{C}$. The magnetic gap is determined by the length of the specimen and, thus, is rather large, about 12.5 mm , giving rise to an inhomogeneous magnetic field along the gap that varies between 110 mT at the ends of the specimen near the gap edges and 15 mT in the gap center. Therefore, the conditions to induce preferential formation of martensite are only fulfilled at the ends of the specimen. Still, this is sufficient to obtain oriented martensite in the whole specimen during temperature cycling similar to the historical effect as mentioned before.

Figure 9. (a) Local strain–temperature characteristics for a Ni–Mn–Ga specimen of $100 \text{ }\mu\text{m}$ thickness and $12 \times 2 \text{ mm}^2$ lateral size upon heating and cooling while a temperature gradient and a magnetic field of 120 mT are applied. In addition, a series of local strain maps are shown in color code that was taken from a test area in the center of the specimen by *in situ* DIC. The propagation of a single austenite—martensite phase front is observed; (b) Same experiment for zero magnetic field; and (c) and (d) Schematics of experimental setup, side and top view. Reprinted with permission from [34], copyright 2014 Elsevier.

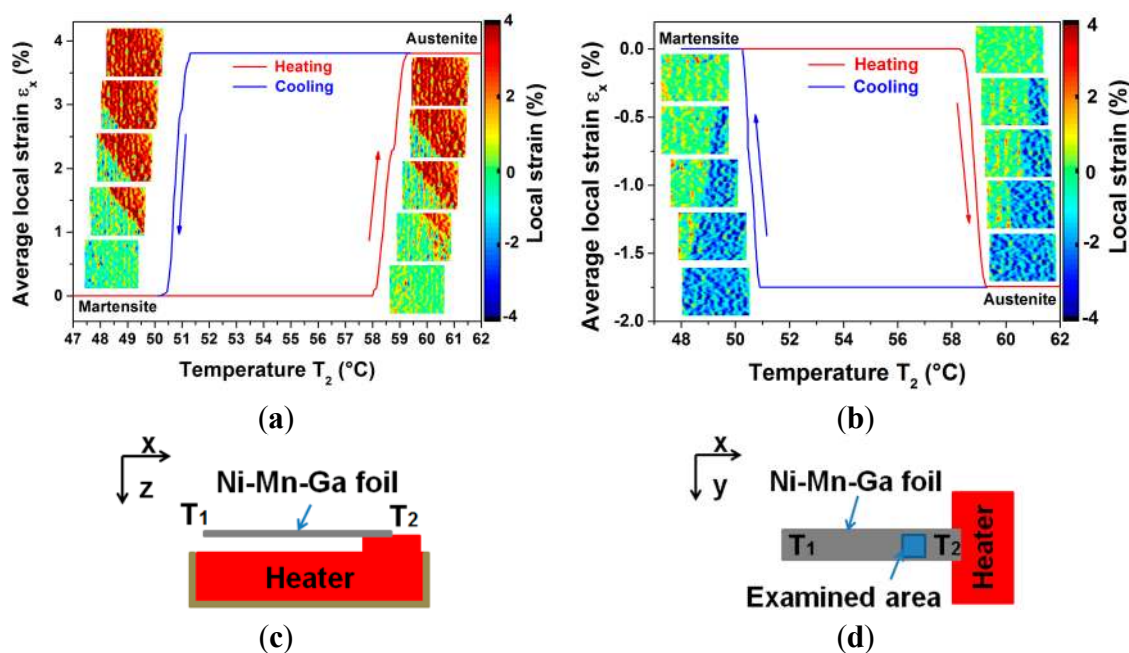


Figure 10. (a) Schematic of actuator setup and (b) photo of a linear actuator using a Ni–Mn–Ga foil of 200 μm thickness in a magnetic circuit. The size of the Ni–Mn–Ga specimen is 12 × 2 mm².

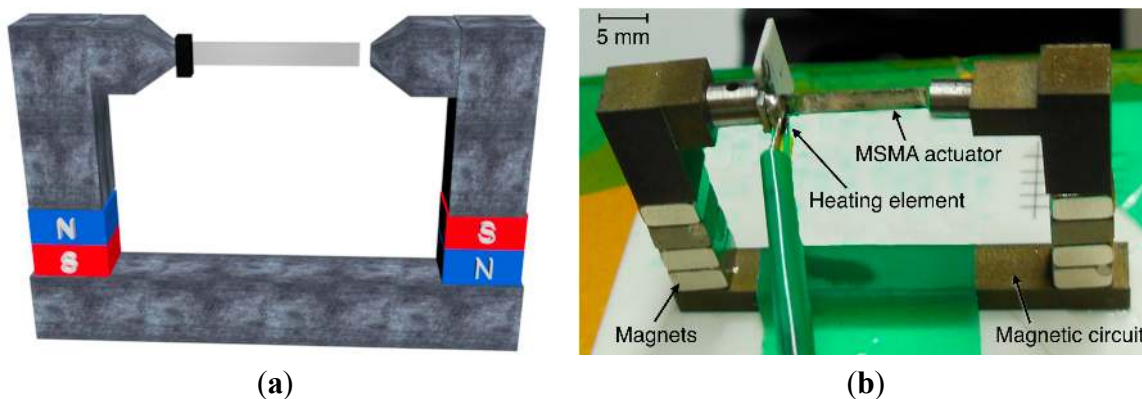
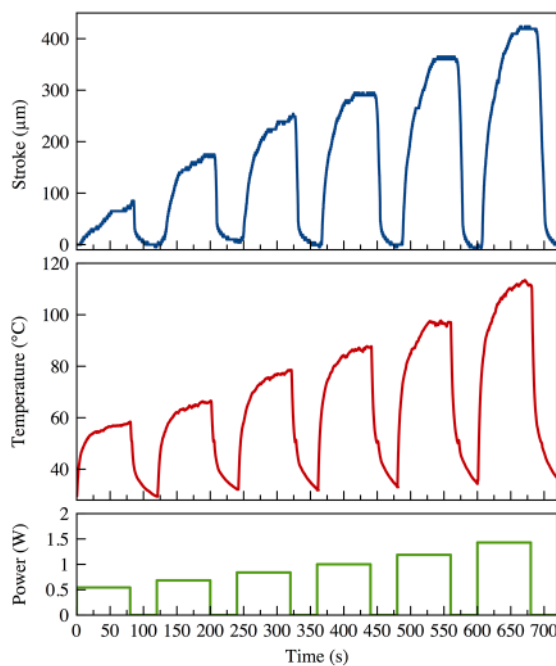


Figure 11 shows a time-resolved actuation characteristic and the corresponding change of temperature at the hot side. The actuator displacement is determined optically with a CCD (charge coupled device) camera by monitoring the position of the freely movable end of the specimen. Once the heating power is turned on, the displacement increases due to nucleation and propagation of a phase boundary along the specimen. For a heating power of 1.54 W, it takes about 70 s to completely move the phase boundary through the specimen and, thus, to induce a complete transformation to austenite. In this case, the hot side heats up to about 100 °C. The maximum displacement is close to the theoretical maximum as discussed before. After switching the heating power off, the temperature drops abruptly within 13 s. Consequently, reset motion is observed due to back propagation of the phase boundary. Depending on the heating power and time of heating pulse, different actuator positions can be excited without the need for an additional sensing scheme.

Figure 11. Time-resolved signals of stroke, temperature at the hot side T_2 , and heating power. The temperature gradient is generated by Joule heating.



The linear actuator presented here is designed to demonstrate the novel actuation principle of single phase boundary actuation, while optimization of heat transfer times is disregarded at this point. Following the design considerations of other thermal MSMA actuation mechanisms as presented in the following, it is clear that heat transfer times can be largely improved depending on the thermal mass of the used Ni–Mn–Ga foil specimen and its thermal interconnection type.

3.3. Bidirectional Magnetostatic and Thermoelastic Actuation

3.3.1. Operation Principle

As can be seen in Figure 2, the temperatures of martensitic transformation and ferromagnetic transition can be tuned by modifying the chemical composition. At the intersection where both temperatures merge, the material undergoes a mixed phase transition in a narrow temperature range from ferromagnetic martensite to paramagnetic austenite upon heating. This unique behavior can be used to control two different forces at the same time. In particular, bidirectional actuation can be generated as sketched in Figure 12 using a polycrystalline Ni–Mn–Ga double beam cantilever placed below a miniature permanent magnet. At low temperatures, the film is in martensitic and ferromagnetic state. In this case, the magnetostatic attraction force F_{mag} dominates, while the biasing force in martensitic state F_{mart} is very low. Therefore, the cantilever is bent in an out-of-plane direction. By applying an electrical heating pulse the cantilever deflects in the opposite direction as the material transforms to paramagnetic austenite, which causes a strong decrease of magnetic attraction force, while at same time the biasing force F_{SMA} strongly increases. Thus, pulsed heating causes a fast oscillatory motion with large deflection angle $\Delta\alpha$ up to 30° rapid cooling occurs due to forced convection during oscillation allowing for high operation frequencies that may exceed 200 Hz depending on the moving mass, see Figure 13. This operation principle nicely represents the concept of smart microactuation using the multifunctional properties in a single piece of MSMA material.

Figure 13 demonstrates the broad frequency response of the microactuator. Below a critical frequency of about 120 Hz, the scanning angle shows several maxima that strongly depend on frequency and heating power. By increasing the driving frequency above 120 Hz, the scanning angle sharply decreases, independently of heating power. This low-pass behavior can be attributed to the dynamics of heat transfer between the double-beam and its environment. The corresponding short time constants are in the ms range, which results from the large surface to volume ratio, the temperature difference of phase transformation and ambient temperature of about 80 K and the forced convective cooling during oscillation. Above about 150 Hz, a broad resonance occurs.

3.3.2. Simulation Model

The rather complex frequency response of the microactuator results from the highly non-linear magnetostatic and shape recovery forces in the system that depend on the dynamic temperature distribution in the double-beam cantilever. During pulsed electrical heating additional Lorentz forces have to be considered that may support or counteract actuator motion. In order to describe the coupled magneto-thermo-mechanical performance, a simulation routine has been developed that executes four independent FEM calculations in a self-consistent way [63]. First, the electrical current distribution is

calculated with an electrical solver, which allows determining the induced heating power. Based on this information, the temperature distribution is calculated in a second time-resolved thermal simulation, taking into account heat conduction, heat convection, and the heat of phase transformation. The temperature data are then transferred to a magnetic solver to calculate magnetic forces that are used in the final mechanical simulation. Several iterations of these calculations are required to obtain self-consistent results.

The single-stage martensitic phase transformation in the MSMA materials is described by a two-phase macromodel [49]. It is a 3D extension of the Tanaka model, which couples a phenomenological macro-scale constitutive law for the relation between stress, strain, temperature and martensitic phase fraction ξ with a kinetic law describing the evolution of ξ as a function of stress and temperature. The effects of geometrical nonlinearity during bending motion are taken into account by the procedure given in [64].

Figure 12. (a) Operation principle of the MSMA microactuator. Legend: N,S—north and south pole of a permanent magnet, F_{mag} —magnetic force, F_{SMA} —shape recovery force, F_{mart} —force in martensitic state, $\Delta\alpha$ —deflection angle. (b) Photo of the MSMA microactuator. The lateral size of the double-beam cantilever is $3 \times 0.4 \text{ mm}^2$. Reprinted with permission from [65], copyright 2006 IOS Press.

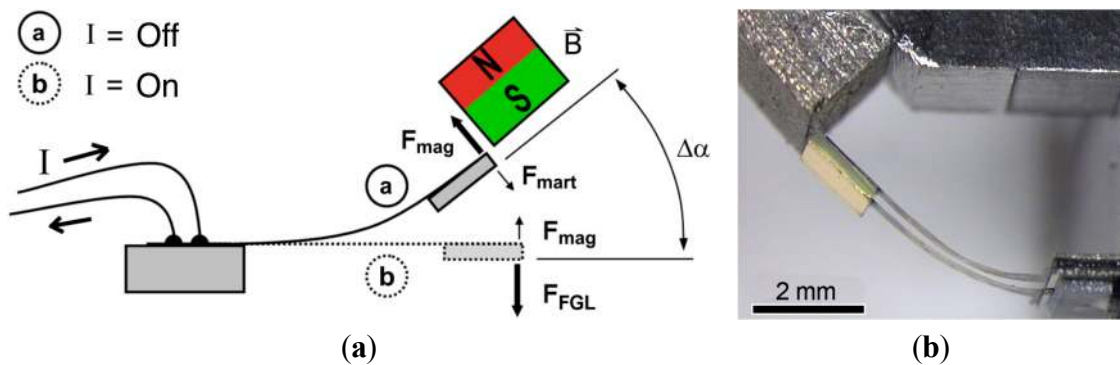


Figure 13. Deflection angle versus frequency of a polycrystalline Ni–Mn–Ga double beam cantilever with lateral size of $3 \times 0.4 \text{ mm}^2$. The duration of heating pulses τ is decreased for increasing frequency f from 1.5 ms ($f < 50 \text{ Hz}$) via 1 ms ($50 < f < 100 \text{ Hz}$) to 0.7 ms ($f > 100 \text{ Hz}$) as indicated.

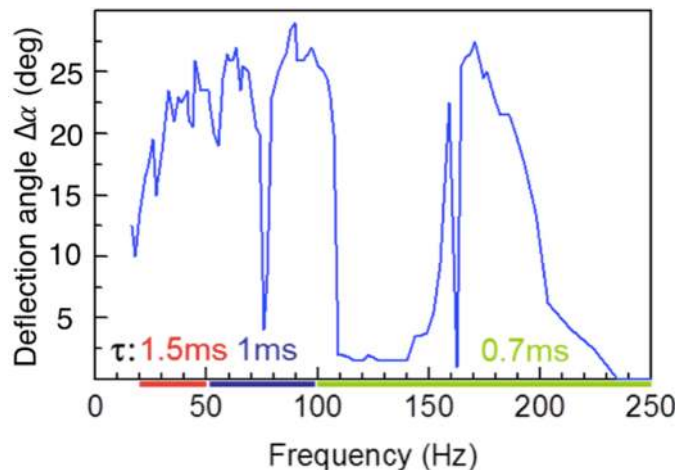
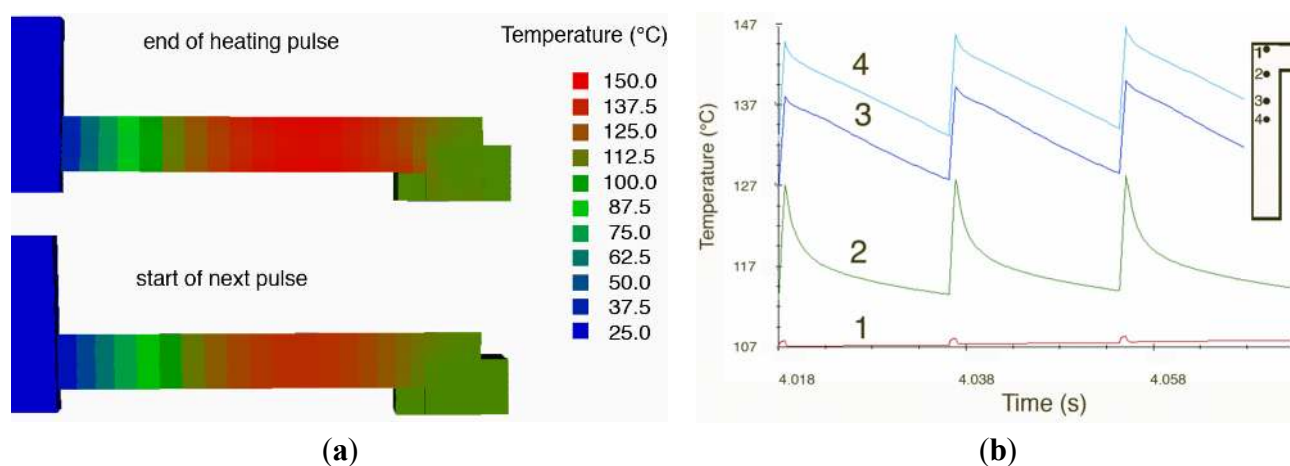


Figure 14a shows a typical temperature distribution along the MSMA beam at the end of a heating pulse and at the beginning of the subsequent heating pulse. The corresponding time-dependent evolution of temperatures at four different locations along the beam cantilever is shown in Figure 14b. These measurements reveal that the temperature varies strongly along the cantilever and that temperature changes keep below about 13 K. Therefore, the average temperatures along the cantilever determine the actuation characteristics. Optimum performance occurs for average temperatures, where the gradients of magnetic and shape recovery force exhibit a maximum. For increasing frequency, the heating power increases as well and Lorentz forces gain importance. In this case, actuation may be either supported or even inhibited depending on whether the Lorentz forces are in or out of phase with the eigenoscillations of the cantilever. This can be seen in Figure 13, where oscillation amplitude is strongly suppressed at about 80 and 160 Hz.

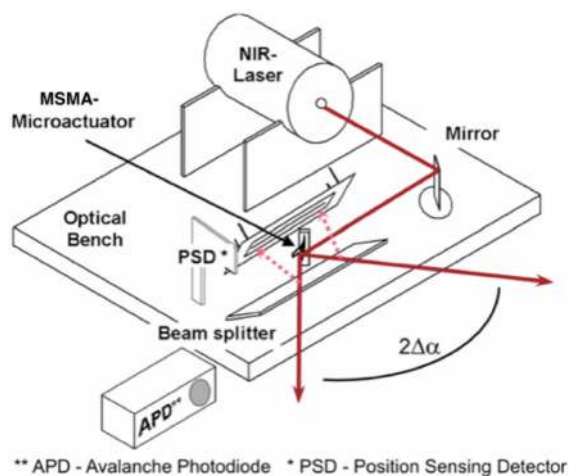
Figure 14. (a) Temperature distribution along one beam of the Ni–Mn–Ga double-beam cantilever at the end of a heating pulse and at the beginning of the subsequent heating pulse; (b) Corresponding time-dependence of temperature for different locations along the cantilever as indicated in the inset. Pulse power, pulse duration, and frequency are 360 mW, 0.7 ms and 55 Hz, respectively. Reprinted with permission from [63], copyright 2006 IOS Press.



3.3.3. Optical Microscanners

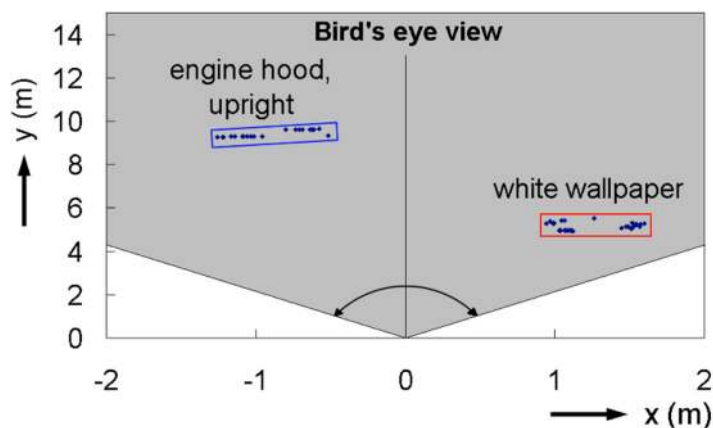
An obvious application of non-resonant actuation of oscillation motion with large deflection angle is optical scanning. 1D optical scanning can be simply realized, e.g., by mounting a micromirror at the front of the MSMA cantilever. Figure 15 shows a setup for 2D optical microscanning that is integrated on a microoptical bench [65]. Main components are a laser diode operated in pulsed mode, the MSMA cantilever, and sensors for deflection angle and distance of the objects to be scanned. During operation, the oscillation of the cantilever and, thus, the deflection characteristic may vary in time due to changing operation conditions. Therefore, optical scanning applications require angular sensing in real time to correlate beam cantilever deflection with the optical scanning angle. Here, the angular sensor consists of a beam splitter that reflects part of the deflected beam and a photodiode array (position sensing detector). Depending on the position of the reflected beam spot, a photo current and subsequently a gained voltage signal is generated, which allows detecting scanning angles with a resolution of 0.1° .

Figure 15. Schematic of the microscanner system. The optical beam path is indicated for the two extreme microactuator positions. Reprinted with permission from [65], copyright 2006 IOS Press.



The distance sensor consists of a time-of-flight detection setup using an avalanche photodiode that measures the time difference between emission and detection of the pulsed laser signals. As illustrated in Figure 16, point clouds are generated based on the data on angle and distance that can be further processed to create object data [65]. In the present example, test demonstrators generated data up to 14 m without and 30 m with collecting optics. This performance is of interest for scanning of unknown objects in space, for instance, scanning the front of mobile systems to detect obstacles [65]. Due to the small size and high performance of the optical microscanner, a wide application potential exists in other fields including environmental control, quality control of surfaces or point-of-care analysis in the medical field.

Figure 16. Point clouds detected by the microscanner system from objects at different angles and distances. The angular range is indicated. Reprinted with permission from [65], copyright 2006 IOS Press.



3.4. Thermomagnetic Actuation

Thermomagnetic actuation makes use of large abrupt changes of magnetization near phase transitions. One example is the thermally induced ferromagnetic transition that is used, e.g., in the

bidirectional actuation principle (Section 3.3) to counteract the shape recovery force. In the following, the change of magnetization of the first order phase transformation between ferromagnetic austenite and non-magnetic martensite in metamagnetic SMA films is considered [66–68].

3.4.1. Operation Principle

Typical metamagnetic SMAs are the quaternary Heusler alloys in the form of Ni–Mn–*X*–*Y* (*X* = Ga, In, Sn, *Y* = Co, Fe, Al). Figure 17 shows a typical magnetization characteristic of a Ni–Co–Mn–In film fabricated by magnetron sputtering [36]. Abrupt changes of magnetization with narrow hysteresis are observed at the transformation temperatures in the range between 85 and 110 °C. In martensitic state below 85 °C, the material is non-magnetic or antiferromagnetic, while it is ferromagnetic in austenitic state at 110 °C. The decrease of magnetization above 110 °C is due to the ferromagnetic transition at T_c . These unique properties of large magnetization in austenitic state and abrupt change of magnetization in a narrow temperature window are highly attractive for thermally induced switching of magnetic forces.

By changing the chemical composition of the film, the magnetization and transition temperatures can be tailored. A suitable method for the search of optimal material compositions is the use of composition spreads in sputtered films instead of using classical bulk metallurgy. By using different targets for every element and controlling the corresponding sputtering power separately, the chemical composition can be controlled with high accuracy [69].

Figure 18 shows the operation principle of thermomagnetic actuation [36]. The demonstrator consists of a polyimide (PI) cantilever that carries a stack of metamagnetic Ni–Co–Mn–In films at its freely movable end. The cantilever is placed in between a miniature magnet and a heat source. While in contact with the heat source in a non-deflected state, the MSMA stack heats above the transformation temperature to ferromagnetic austenite causing the cantilever to bend in out-of-plane direction due to ferromagnetic attraction. Upon cooling to non-magnetic martensite, the magnetic attraction force vanishes and the elastic reset force of the PI cantilever restores the initial undeflected state.

Figure 17. Thermo-magnetization characteristic of a Ni–Co–Mn–In film for a magnetic field of 3 T. The start and finish temperatures of forward and reverse transformation between martensite (M) and austenite (A) are indicated by arrows.

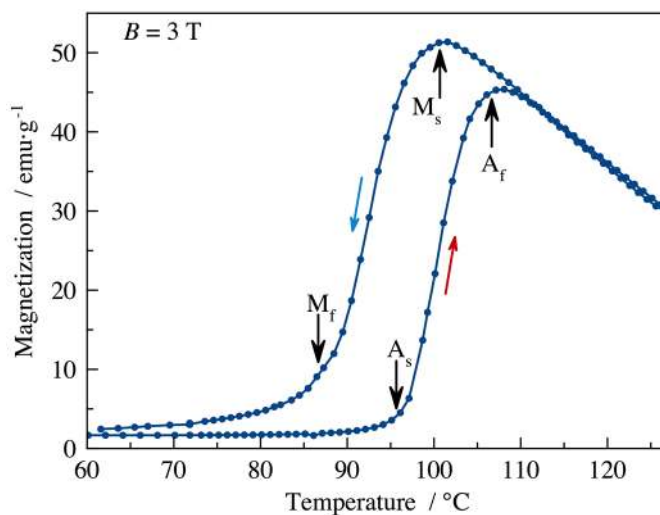
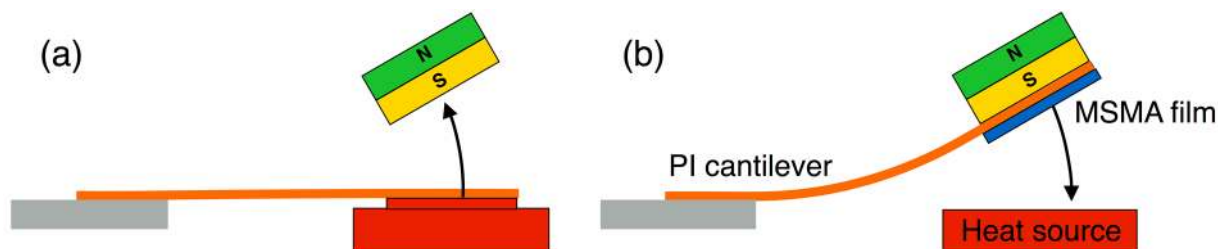


Figure 18. Operation principle of thermomagnetic actuation. The system consists of a polyimide (PI) cantilever fixed on a substrate, a stack of metamagnetic SMA films at the freely movable cantilever end, a magnet and a heat source. (a) A magnetostatic attraction force occurs due to phase transformation to ferromagnetic austenite while in contact to the heat source; (b) The elastic reset force dominates after cooling to nonmagnetic martensite. Adapted from [70].



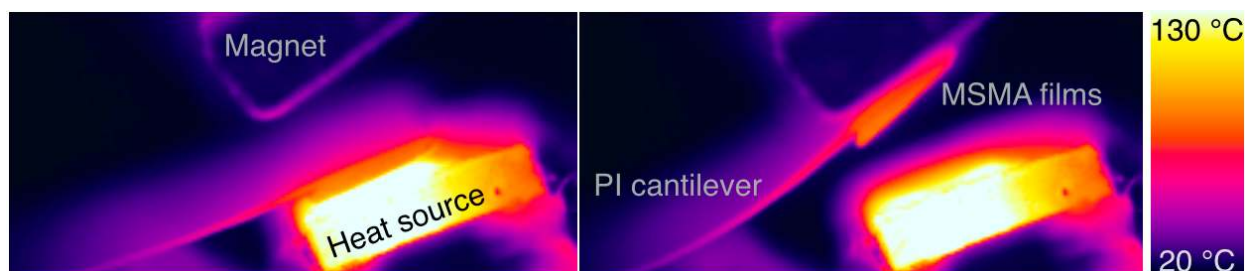
3.4.2. Thermomagnetic Microswitches

The presented mechanism is of interest for thermomagnetic actuation and temperature sensing. First demonstrators have been developed for thermomagnetic switching based on the setup shown in Figure 18 using a PI cantilever with integrated metamagnetic SMA films [70]. The films have been fabricated by dual magnetron sputtering of a $\text{Ni}_{45}\text{Mn}_{40}\text{In}_{15}$ target and a 99.9 wt % Co target at sputtering powers of 200 W RF (radio-frequency) and 8 W DC (direct current), respectively. The final composition, determined by the inductive coupled plasma method, was $\text{Ni}_{50.4}\text{Co}_{3.7}\text{Mn}_{32.8}\text{In}_{13.1}$. The films are sputtered on sacrificial polyvinyl alcohol (PVA) substrates that can be dissolved after sputtering. Crystallization of the freestanding 5 μm thick films is performed by heat treatment at 900 $^{\circ}\text{C}$ for one hour. A demonstrator is developed using a 25 μm thick PI cantilever of $2 \times 4 \text{ mm}^2$ size. Ten Ni–Co–Mn–In films are structured to $1 \times 1.5 \text{ mm}^2$ specimens by laser cutting and mounted on the cantilever tip.

Time-dependent deflection and infrared thermography measurements have been performed simultaneously to analyze the thermo-magneto-mechanical performance [70]. Figure 19 shows IR (infrared) thermography profiles of the front part of the demonstrator in the extreme positions at the heat source and at the magnet. The temperature of the heat source has been set to 130 $^{\circ}\text{C}$. The magnet is at room temperature and therefore acts as a heat sink. In the present case, thermomagnetic switching occurs at a frequency of about 2 Hz. Thereby, the temperature of the metamagnetic SMA stack shows a periodic temperature change of about 8 K. The actuation principle works in a broad temperature range above the austenite finish temperature of 103 $^{\circ}\text{C}$. The main effect of increasing the temperature of the heat source is to accelerate the heat transfer due to the larger temperature gradient. Since the cantilever leaves the heat source as soon as the stack heats above A_f , overheating of the cantilever tip is prevented even at high heat source temperatures.

It is interesting to note that the demonstrator may also be operated in resonance at much faster switching cycles. This is enabled by shifting the magnet beyond the tip of the cantilever allowing for free movement of the cantilever tip along the edge of magnet. In this case, thermal actuation is up-converted to an oscillatory motion at the much larger Eigen frequency of 160 Hz [70].

Figure 19. Time-resolved IR thermography measurement of the thermomagnetic microactuator when in contact to the heat source (left) and to the magnet (right). Adapted from [70].



3.5. Magnetic Stray-Field Actuation

Epitaxial FSMA films show another actuation mechanism based on the magnetic stray-field-induced microstructure [37]. When transforming a ferromagnetic austenite film to the martensite phase, variants with their easy axis in the film plane are preferentially formed in order to avoid magnetostatic energy contributions. Magnetocrystalline anisotropy favors the alignment of magnetization along the easy axis. However, variants with their easy magnetization axis perpendicular to the film plane create a large magnetic stray field. This is not the case if both variants align with their easy axis in-plane. In this case, the formation of magnetic domains allows flux closure and reduces magnetostatic energy. The additional stray-field energy contribution hence disfavors variants with the easy axis out-of-plane. Experiments on epitaxial Ni–Mn–Ga films show that an almost even distribution of only the two energetically favored in-plane variants is forming upon cooling. The lattice difference between the austenitic state and the preferentially aligned martensite variants in the martensitic state gives rise to the theoretical maximum strain of 1.1%.

This actuation mechanism is similar to the conventional two-way shape-memory effect, yet neither training nor an external magnetic field is required. The mechanism benefits from the combination of ferromagnetic and martensitic properties that is only present in MSMA materials. Due to the finite size of magnetic domains, it is a unique feature of small systems. For possible applications, it is sufficient to pass a heating current through the film. Thus, magnetic stray-field actuation may be an interesting option for application in sub-micrometer dimensions. So far, this actuation mechanism has not been implemented in a demonstrator device.

4. Conclusions

This review presents an overview of MSMA microactuators, their underlying actuation mechanisms, engineering issues and fabrication technologies. Using MSMA films and foils for microactuation and sensing is very attractive as they enable multifunctional performance in a compact device. Thanks to their good scaling behavior, MSMA microactuators can be miniaturized to a large extent without losing their unique performance properties. Thereby, the intrinsic disadvantage of long time constants upon thermal actuation is strongly improved as well.

MSMA films and foils with various chemical compositions have been developed up to now. The combination of these materials with micromachining and integration technologies opens up the

possibility to realize a new generation of smart MEMS devices. Key enabling technologies have been novel bonding and substrate release technologies on the wafer scale. As a consequence, the feasibility to fabricate various types of MSMA microactuators has been demonstrated introducing new disruptive designs and mechanisms. First MSM linear actuators, optical microscanners, and metamagnetic microswitches have been presented showing promising specifications. More importantly, their simple design opens up much room for further downscaling in size. Future challenges are concerned with the development of a larger variety of MSMA films with low twinning stress, the full integration of MSMA materials in state-of-the art MEMS devices including microelectronics as well as the wide-spread allocation of simulation and optimization tools.

So far, MSMA microactuators are still in an early development stage. The performance of first demonstrators provides the drives for further research and development. The prospects are new emerging MEMS applications.

Acknowledgments

The authors thank the German Science Foundation (DFG) for funding via the Priority Program SPP1239 Magnetic Shape as well as the projects FACTS and Thervest. Part of the work has been funded within the sixth framework of the European Commission via the project Q2M.

Author Contributions

Manfred Kohl developed the concepts, designed the experiments and wrote the manuscript. Berthold Krevet and Frank Wendler conducted the FEM simulations, Marcel Gueltig, Viktor Pinneker and Ruizhi Yin investigated the thermomagnetic actuation, single-phase boundary actuation and MSM actuation, respectively.

Conflicts of Interest

The authors declare no conflict of interest.

References

1. Webster, P.J.; Ziebeck, K.R.A. Heusler alloys. In *Alloys and Compounds of d-Elements with Main Group Elements. Part 2. Landolt-Börnstein—Group III Condensed Matter*; Springer-Verlag: Berlin, Germany, 1988; pp. 75–79.
2. Kohl, M.; Reddy, Y.S.; Khelifaoui, F.; Krevet, B.; Backen, A.; Fähler, S.; Eichhorn, T.; Jakob, G.; Mecklenburg, A. Recent progress in FSMA microactuator developments. *Mater. Sci. Forum* **2010**, *635*, 145–154.
3. Bhattacharya, K.; James, R.D. The material is the machine. *Science* **2005**, *307*, 53–54.
4. Ullakko, K.; Huang, J.K.; Kantner, C. Large magnetic-field-induced strains in Ni₂MnGa single crystals. *Appl. Phys. Lett.* **1996**, *69*, 1966–1968.
5. Müllner, P.; Chernenko, V.A.; Kosterz, G. Stress-induced twin rearrangement resulting in change of magnetization in a Ni–Mn–Ga ferromagnetic martensite. *Scr. Mater.* **2003**, *49*, 129–133.

6. Mañosa, L.; González-Alonso, D.; Planes, A.; Bonnot, E.; Barrio, M.; Tamarit, J.L.; Aksoy, S.; Acet, M. Giant solid-state barocaloric effect in the Ni–Mn–In magnetic shape-memory alloy. *Nat. Mater.* **2010**, *9*, 478–481.
7. Planes, A.; Mañosa, L.; Acet, M. Magnetocaloric effect and its relation to shape-memory properties in ferromagnetic heusler alloys. *J. Phys. Condens. Matter* **2009**, *21*, doi:10.1088/0953-8984/21/23/233201.
8. Chernenko, V.A.; Ohtsuka, M.; Kohl, M.; Khovailo, V.V.; Takagi, T. Transformation behavior of Ni–Mn–Ga thin films. *Smart Mater. Struct.* **2005**, *14*, S245–S252.
9. Khelifaoui, F.; Kohl, M.; Szabo, V.; Mecklenburg, A.; Schneider, R. Development of single crystalline Ni–Mn–Ga foil microactuators. In *International Conference on Martensitic Transformations (ICOMAT) 2008*; Olsen, G.B., Lieberman, D.S., Saxena, A., Eds.; John Wiley and Sons: Hoboken, NJ, USA, 2013; pp. 215–222.
10. Heczko, O.; Soroka, A.; Hannula, S.P. Magnetic shape memory effect in thin foils. *Appl. Phys. Lett.* **2008**, *93*, doi:10.1063/1.2957675.
11. Dong, J.W.; Chen, L.C.; Xie, J.Q.; Muller, T.; Carr, D.M.; Palmstrøm, C.J.; McKernan, S.; Pan, Q.; James, R.D. Epitaxial growth of ferromagnetic Ni₂MnGa on GaAs (001) using NiGa interlayers. *J. Appl. Phys.* **2000**, *88*, 7357–7359.
12. Thomas, M.; Heczko, O.; Buschbeck, J.; Röbller, U.K.; McCord, J.; Scheerbaum, N.; Schultz, L.; Fähler, S. Magnetically induced reorientation of martensite variants in constrained epitaxial Ni–Mn–Ga films grown on MgO (001). *New J. Phys.* **2008**, *10*, doi:10.1088/1367-2630/10/2/023040.
13. Jakob, G.; Elmers, H.J. Epitaxial films of the magnetic shape memory material. *J. Magn. Magn. Mater.* **2007**, *310*, 2779–2781.
14. Backen, A.; Yeduru, S.R.; Diestel, A.; Schultz, L.; Kohl, M.; Fähler, S. Epitaxial Ni–Mn–Ga Films for Magnetic Shape Memory Alloy Microactuators. *Adv. Eng. Mater.* **2012**, *14*, 696–709.
15. Chernenko, V.A. Compositional instability of beta-phase in Ni–Mn–Ga alloys. *Scr. Mater.* **1999**, *40*, 523–527.
16. Lanska, N.; Soderberg, O.; Sozinov, A.; Ge, Y.; Ullakko, K.; Lindroos, V.K. Composition and temperature dependence of the crystal structure of Ni–Mn–Ga alloys. *J. Appl. Phys.* **2004**, *95*, 8074–8078.
17. Murray, S.J.; Marioni, M.A.; Kukla, A.M.; Robinson, J.; Handley, R.C.O.; Allen, S.M. Large field induced strain in single crystalline Ni–Mn–Ga ferromagnetic shape memory alloy. *J. Appl. Phys.* **2000**, *87*, 5774–5776.
18. Ohtsuka, M.; Itagaki, K. Effect of heat treatment on properties of Ni–Mn–Ga films prepared by a sputtering method. *Int. J. Appl. Electromagn. Mech.* **2000**, *12*, 49–59.
19. Castaño, F.J.; Nelson-Cheeseman, B.; O’Handley, R.C.; Ross, C.A.; Redondo, C.; Castaño, F. Structure and thermomagnetic properties of polycrystalline Ni–Mn–Ga thin films. *J. Appl. Phys.* **2003**, *93*, 8492–8494.
20. Hakola, A.; Heczko, O.; Jaakola, A.; Kajava, T.; Ullakko, K. Ni–Mn–Ga films on Si, GaAs and Ni–Mn–Ga single crystals by pulsed laser deposition. *Appl. Surf. Sci.* **2004**, *238*, 155–158.
21. Ohtsuka, M.; Konno, Y.; Matsumoto, M.; Takagi, T.; Itagaki, K. Magnetic-field induced two-way shape memory effect of ferromagnetic Ni₂MnGa sputtered films. *Mater. Trans.* **2006**, *47*, 625–630.

22. Besseghini, S.; Gambardella, A.; Chernenko, V.A.; Hagler, M.; Pohl, C.; Muellner, P.M.; Ohtsuka, M.; Doyle, S. Transformation behavior of Ni–Mn–Ga/Si(100) thin film composites with different film thicknesses. *Eur. Phys. J. Spec. Top.* **2008**, *158*, 179–185.
23. Chernenko, V.A.; Lopez Anton, R.; Barandiaran, J.M.; Orue, I.; Besseghini, S.; Ohtsuka, M.; Gambardella, A. MFM Domain Imaging of Textured Ni–Mn–Ga/MgO(100) Thin Films. *IEEE Trans. Magn.* **2008**, *44*, 3040–3043.
24. Golub, V.; Reddy, K.M.; Chernenko, V.; Muellner, P.; Punnoose, A.; Ohtsuka, M. Ferromagnetic resonance properties and anisotropy of Ni–Mn–Ga thin films of different thicknesses deposited on Si substrate. *J. Appl. Phys.* **2009**, *105*, doi:10.1063/1.3075395.
25. Dong, J.W.; Xie, J.Q.; Lu, J.; Adelman, C.; Palmstrøm, C.J.; Cui, J.; Pan, Q.; Shield, T.W.; James, R.D.; McKernan, S. Shape memory and ferromagnetic shape memory effects in single-crystal Ni₂MnGa thin films. *J. Appl. Phys.* **2004**, *95*, 2593–2600.
26. Zhang, Y.; Hughes, R.A.; Britten, J.F.; Gong, W.; Preston, J.S.; Botton, G.A.; Niewczas, M. Epitaxial Ni–Mn–Ga films derived through high temperature *in situ* depositions. *Smart Mater. Struct.* **2009**, *18*, doi:10.1088/0964-1726/18/2/025019.
27. Tillier, J.; Bourgault, D.; Odier, P.; Ortega, L.; Pairis, S.; Fruchart, O.; Caillault, N.; Carbone, L. Tuning macro-twinned domain sizes and the b-variants content of the adaptive 14-modulated martensite in epitaxial Ni–Mn–Ga films by co-sputtering. *Acta Mater.* **2011**, *59*, 75–81.
28. Backen, A.; Yeduru, S.R.; Kohl, M.; Baunack, S.; Diestel, A.; Holzappel, B.; Schultz, L.; Fähler, S. Comparing properties of substrate-constrained and freestanding epitaxial Ni–Mn–Ga films. *Acta Mater.* **2010**, *58*, 3415–3421.
29. Yeduru, S.R.; Backen, A.; Kübel, C.; Wang, D.; Scherer, T.; Fähler, S.; Schultz, L.; Kohl, M. Microstructure of free-standing epitaxial Ni–Mn–Ga films before and after variant reorientation. *Scr. Mater.* **2012**, *66*, 566–569.
30. Grund, T.; Guerre, R.; Despont, M.; Kohl, M. Transfer bonding technology for batch fabrication of SMA microactuators. *Eur. Phys. J. Spec. Top.* **2008**, *158*, 237–242.
31. Grund, T.; Cuntz, T.; Kohl, M. Batch fabrication of polymer microsystems with shape memory microactuators. In Proceedings of IEEE 21st International Conference on Micro Electro Mechanical Systems, Tucson, AZ, USA, 13–17 January 2008; pp. 423–426.
32. Barth, J.; Megnin, C.; Kohl, M. A bistable shape memory alloy microvalve with magnetostatic latches. *J. Microelectromech. Syst.* **2012**, *21*, 76–84.
33. Megnin, C.; Kohl, M. Shape memory alloy microvalves for a fluidic control system. *J. Micromech. Microeng.* **2014**, *24*, doi:10.1088/0960-1317/24/2/025001.
34. Pinneker, V.; Gueltig, M.; Sozinov, A.; Kohl, M. Single phase boundary actuation of a ferromagnetic shape memory foil. *Acta Mater.* **2014**, *64*, 179–187.
35. Kohl, M.; Brugger, D.; Ohtsuka, M.; Takagi, T. A novel actuation mechanism on the basis of ferromagnetic SMA thin films. *Sens. Actuators A* **2004**, *114*, 445–450.
36. Gueltig, M.; Ossmer, H.; Ohtsuka, M.; Miki, H.; Tsuchiya, K.; Takagi, T.; Kohl, M. High frequency thermal energy harvesting using magnetic shape memory films. *Adv. Energy Mater.* **2014**, doi:10.1002/aenm.201400751.

37. Thomas, M.; Heczko, O.; Buschbeck, J.; Lai, Y.W.; McCord, J.; Kaufmann, S.; Schultz, L.; Faehler, S. Stray-field-induced actuation of free-standing magnetic shape-memory films. *Adv. Mater.* **2009**, *21*, 3708–3711.
38. Heczko, O. Magnetic shape memory effect and magnetization reversal. *J. Magn. Magn. Mater.* **2005**, *290*, 787–794.
39. Straka, L.; Hanninen, H.; Heczko, O. Temperature dependence of single twin boundary motion in Ni–Mn–Ga martensite. *Appl. Phys. Lett.* **2011**, *98*, doi:10.1063/1.3573860.
40. Suorsa, I.; Tellinen, J.; Pagounis, E.; Aaltio, I.; Ullakko, K. Applications of magnetic shape memory actuators. In Proceedings of Actuator 2002, Bremen, Germany, 10–12 June 2002; pp. 158–161.
41. Tellinen, J.; Suorsa, I.; Jääskeläinen, A.; Aaltio, I. Basic properties of magnetic shape memory actuators. In Proceedings of Actuator 2002, Bremen, Germany, 10–12 June 2002; pp. 10–12.
42. Faran, E.; Shilo, D. The kinetic relation for twin wall motion in NiMnGa. *J. Mech. Phys. Solids* **2011**, *59*, 975–987.
43. Sozinov, A.; Lanska, N.; Soroka, A.; Zou, W. 12% magnetic field-induced strain in Ni–Mn–Ga-based non-modulated martensite. *Appl. Phys. Lett.* **2013**, *102*, doi:10.1063/1.4775677.
44. Murray, S.J.; Marioni, M.; Allen, S.M.; O’Handley, R.C.; Lograsso, T.A. 6% magnetic-field-induced strain by twin-boundary motion in ferromagnetic Ni–Mn–Ga. *Appl. Phys. Lett.* **2000**, *77*, 886–888.
45. Kohl, M.; Krevet, B.; Yeduru, S.R.; Ezer, Y.; Sozinov, A. A novel foil actuator using the magnetic shape memory effect. *Smart Mater. Struct.* **2011**, *20*, doi:10.1088/0964-1726/20/9/094009.
46. James, R.D.; Wuttig, M. Magnetostriction of martensite. *Philos. Mag. A* **1998**, *77*, 1273–1299.
47. Likhachev, A.A.; Ullakko, K. Quantitative model of large magnetostrain effect in ferromagnetic shape memory alloys. *Eur. Phys. J. B* **2000**, *14*, 263–267.
48. Kiefer, B.; Lagoudas, D.C. Modeling the coupled strain and magnetization response of magnetic shape memory alloys under magnetomechanical loading. *J. Intell. Mater. Syst. Struct.* **2009**, *20*, 143–170.
49. Kohl, M.; Krevet, B. 3D simulation of a shape memory microactuator. *Mater. Trans.* **2002**, *43*, 1030–1036.
50. O’Handley, R.C. Model for strain and magnetization in magnetic shape-memory alloys. *J. Appl. Phys.* **1998**, *83*, 3263–3270.
51. Hirsinger, L.; Lexcellent, C. Internal variable model for magneto-mechanical behaviour of ferromagnetic shape memory alloys Ni–Mn–Ga. *J. Phys. IV France* **2003**, *112*, 977–980.
52. Lee, K.L.; Seelecke, S. A model for ferromagnetic shape memory thin film actuators. *Smart Struct. Mater.* **2005**, *5757*, 302–313.
53. Krevet, B.; Kohl, M. FEM simulation of a Ni–Mn–Ga film bridge actuator. *Physics Procedia* **2010**, *10*, 154–161.
54. Krevet, B.; Pinneker, V.; Kohl, M. A magnetic shape memory foil actuator loaded by a spring. *Smart Mater. Struct.* **2012**, *21*, doi:10.1088/0964-1726/21/9/094013.
55. Krevet, B.; Kohl, M.; Morrison, P.; Seelecke, S. Magnetization- and strain-dependent free energy model for FEM simulation of magnetic shape memory alloys. *Eur. Phys. J. Spec. Top.* **2008**, *158*, 205–211.
56. Krevet, B.; Kohl, M. Modeling and FEM simulation of shape memory microactuators. *Mater. Sci. Forum* **2008**, *583*, 229–256.

57. Krevet, B.; Kohl, M. Thermodynamic modelling of ferromagnetic shape memory actuators. *Mater. Sci. Forum* **2009**, *635*, 175–180.
58. Pinneker, V.; Krevet, B.; Ezer, Y.; Sozinov, A.; Kohl, M. A Ni–Mn–Ga foil actuator based on the magnetic shape memory effect. In Proceedings of Actuator 2012, Bremen, Germany, 18–20 June 2012; pp. 332–335.
59. Niskanen, A.J.; Soroka, A. Proportional control and self-sensing in a magnetic shape memory (MSM) alloy actuator. In Proceedings of Actuator 2012, Bremen, Germany, 18–20 June 2012; pp. 276–278.
60. Srivastava, V.K.; Chatterjee, R.; O’Handley, R.C. Effect of twin boundaries on electrical transport in a Ni–Mn–Ga single crystal. *Appl. Phys. Lett.* **2006**, *89*, doi:10.1063/1.2397541.
61. Zeng, M.; Cai, M.Q.; Or, S.W.; Chan, H.L.W. Anisotropy of the electrical transport properties in a Ni₂MnGa single crystal: Experiment and theory. *J. Appl. Phys.* **2010**, *107*, doi:10.1063/1.3354105.
62. Suorsa, I.; Pagounis, E.; Ullakko, K. Position dependent inductance based on magnetic shape memory materials. *Sens. Actuators A* **2005**, *121*, 136–141.
63. Krevet, B.; Kohl, M.; Brugger, D. Coupled simulation of the thermo-magneto-mechanical properties of a Ni–Mn–Ga actuator. *Int. J. Appl. Electromagn. Mech.* **2006**, *23*, 125–131.
64. Krevet, B.; Kohl, M. Finite element simulation of SMA microactuators with large deflection. *J. Phys. IV France* **2004**, *115*, 365–373.
65. Brugger, D.; Kohl, M.; Hollenbach, U.; Kapp, A.; Stiller, C. Ferromagnetic shape memory microscanner system for automotive applications. *Int. J. Appl. Electromagn. Mech.* **2006**, *23*, 107–112.
66. Kainuma, R.; Imano, Y.; Ito, W.; Morito, H.; Sutou, Y.; Oikawa, K.; Fujita, A.; Ishida, K.; Okamoto, S.; Kitakami, O.; *et al.* Magnetic-field-induced shape recovery by reverse phase transformation. *Nature* **2006**, *439*, 957–960.
67. Niemann, R.; Heczko, O.; Schultz, L.; Fähler, S. Metamagnetic transitions and magnetocaloric effect in epitaxial Ni–Co–Mn–In films. *Appl. Phys. Lett.* **2010**, *97*, doi:10.1063/1.3517443.
68. Srivastava, V.; Chen, X.; James, R.D. Hysteresis and unusual magnetic properties in the singular Heusler alloy Ni₄₅Co₅Mn₄₀Sn₁₀. *Appl. Phys. Lett.* **2010**, *97*, doi:10.1063/1.3456562.
69. Zarnetta, R.; Takahashi, R.; Young, M.L.; Savan, A.; Furuya, Y.; Thienhaus, S.; Maaß, B.; Rahim, M.; Frenzel, J.; Brunken, H.; *et al.* Identification of quaternary shape memory alloys with near-zero thermal hysteresis and unprecedented functional stability. *Adv. Funct. Mater.* **2010**, *20*, 1917–1923.
70. Gueltig, M.; Ossmer, H.; Ohtsuka, M.; Miki, H.; Tsuchiya, K.; Takagi, T.; Kohl, M. Thermomagnetic actuation by low hysteresis metamagnetic Ni–Co–Mn–In films. *Mater. Today*, submitted for publication.